Hierarchical Urchin-like $Cu_xCo_{3-x}O_4$ Spinels as Oxygen Evolution Reaction Catalysts in Alkaline Anion Exchange Membrane Water Electrolyzers

Rose Anne Acedera[a], Gaurav Gupta[b,c], Mohamed Mamlouk[b], Kodai Kawano[d], Yagi Shunsuke[d], and Mary Donnabelle Balela[a,*]

[a] *Sustainable Electronic Materials Group, Department of Mining, Metallurgical, and Materials Engineering, University of the Philippines Diliman, Diliman 1101, Quezon City, Philippines*

[b] *School of Engineering, Newcastle University, Newcastle upon Tyne, United Kingdom NE1 7RU*

[c] *Department of Enginering, Lancaster University, Lancaster, United Kingdom LA1 4YW*

[d] *Institute of Industrial Science, University of Tokyo, Komaba Meguro-ku, Tokyo, Japan 153-8505*

[*]Corresponding author.

Tel. No: +632-9818500 loc. 3132

E-mail address: mlbalela1@up.edu.ph

Abstract

In this work, powdered hierarchical $Cu_xCo_{3-x}O_4$ catalysts were used as catalysts for the oxygen evolution reaction (OER) in an alkaline anion exchange membrane water electrolyzer (AAEMWE). The effect of increasing Cu concentration (x = 0, 0.25, 0.5, 0.75, and 1) on the OER catalysis performance of the spinel Co_3O_4 was studied. In general, Cu-doped Co_3O_4 samples performed better than the undoped spinel catalyst. The sample synthesized with Cu-doping at x = 0.75 (CCO-0.75) performed the best among the catalysts tested with an overpotential of 385 mV at 10 mA cm^{-2} in 1 M KOH, which is 24% lower than that recorded for the undoped Co_3O_4 sample. An AAEMWE was assembled using CCO-0.75 on Ti gas diffusion layer (GDL), and Pt/C on carbon GDL as the anode, and cathode, respectively. The CCO-0.75|| Pt/C cell required only 1.65 V to reach 100 mA cm^{-2} at 60 °C in 1 M KOH.

1. Introduction

Renewable energy sources (RES), such as solar, hydropower, geothermal, wind, and biomass, are gaining increasing importance in the global energy mix [1]. However, the highly variable and intermittent nature of these resources result in the mismatch between the energy demand, and the energy supply from the RES. This mismatch necessitates the integration of efficient energy storage and conversion systems to RES [2].

Water electrolysis stands as a viable energy storage method [3]. In this technology, water may be broken down into O_2 and H_2 through the application of an electrical potential coming from renewable sources [4]. Subsequently, the produced gases will be fed into a fuel cell, which when operated releases energy. Additionally, H_2 is an energy-dense fuel that can instantaneously release stored energy without producing harmful by-products, rendering it as an ideal energy storage medium [5].

Water splitting can occur under different reaction conditions, namely in aqueous alkaline or acidic electrolytes at low to moderate temperatures, or with solid oxide electrolytes at high temperatures. Depending on the type of the electrolyte, and on the working temperature, water electrolysis cells can be classified as alkaline, proton exchange membrane (PEM), and solid oxide (SO) electrolysis cell. Among these technologies, alkaline water electrolysis (AWE) is the most commonly used in the industry owing to its low operational cost, environmental soundness, and highly stable operation [6–9]. Electrolysis under acidic conditions using a PEM tends to be more corrosive to the electrolyzer components, particularly the electrodes, than alkaline environments. This increased degree of corrosion can lead to the gradual degradation of the electrodes, compromising the overall integrity of the electrolysis system. To mitigate this issue, Pt group metals are commonly used as the electrode materials However, this choice increases both capital and operational expenditures needed to build and maintain the electrolyzer. In terms of performance, PEMWEs have achieved higher efficiencies and current

3

A particular point of improvement in AWEs involves reevaluating the usage of concentrated electrolyte KOH solutions, which brings up issues on the purity of the produced H_2 due to the crossing over of the gases across the liquid electrolyte and causes difficulties in fabricating the cell. To resolve such concerns, alkaline anion exchange membranes (AAEMs) are now being used as the electrolyte instead of the liquid KOH solution [11]. The more compact structure of the AAEMs makes AWEs easier to use and reduces the electrolyte resistance, hence making the alkaline anion exchange membrane water electrolyzers (AAEMWEs) outperform the conversion efficiency of the conventional AWEs.

To make AAEMWE even more competitive over other electrolysis technologies, the development of high performance electrodes, especially the anode, is a key consideration [6,12]. In alkaline electrolysis, the formation of O_2 occurs through the oxidation of the hydroxyl ions (OH⁻) to O_2 as in, $4\ OH^-_{(aq)} \rightarrow O_{2\,(g)} + 2\ H_2O + 4\ e^-$. This oxygen evolution reaction (OER), which occurs at the anode of water electrolyzers, is catalytically-demanding. OER proceeds through a number of different pathways and involves the multi-step transfer of four electrons regardless of the mechanism followed [13]. To reduce the high overpotentials encountered in OER and hasten the reaction kinetics, the development of efficient catalytic electrodes is critical.

Noble metal-based catalysts are the most studied materials for OER electrocatalysis due to their superior activity. OER activity was found to improve in the order: Pt < Pd < Ir < Ru [14–17]. As such, Ir and Ru, as well as their oxides IrO_2 and RuO_2, are at the forefront of OER electrocatalysts, with very low overpotentials and Tafel slopes [18–20]. Although these noble

metal-based catalysts show superior OER electrocatalytic performance, their scarcity, thus high cost, and poor stability under alkaline environment limit their industrial applications [21]. To minimize the dependence on noble metal-based catalysts, extensive research has been carried out to look for alternative electrocatalysts for OER [22,23]. Carbon-based materials [24,25], metal phosphides [26–28], sulfides [27–29], layered double hydroxides, and hydroxides [32–35] show promising OER performance. However, due to their poor stability in alkaline medium, transition metal oxides, specifically spinel oxides, have been considered to be among the best alternatives to noble metal-based catalysts [36,37].

Cobalt (II, III) oxide (Co_3O_4) proves to be one of the best OER electrocatalyst among the transition metal spinel oxides [38]. Co_3O_4 exhibits high activity for OER and high stability in strong alkaline media while being less expensive, readily available, and environmentally-friendly [11,39]. However, it exhibits low to moderate electrical conductivity due to its semiconducting nature. To improve the electrical behavior of Co_3O_4, metal doping is a promising route [40,41]. Some of the viable dopants identified in literature include Ni [38,42,43], Li [44], Mn [45,46], and Cu [39,47,48]. While these dopants provide the possibility of improving the electrocatalytic activity of Co_3O_4 towards OER, Cu has been regarded as one of the most viable dopants because of its cost-effectivity [11,39,47,49]. Even more, a study on the catalytic behavior of M-doped Co_3O_4 (M = Li, Ni, Cu) reported an increase in OER activity in the order $Co_3O_4 < Ni_xCo_{3-x}O_4 << Cu_xCo_{3-x}O_4 < Li_x Co_{3-x}O_4$ [44]. Despite this potential, only a few articles report the use of Cu-doped Co_3O_4 as anode electrode materials for AAEMWE [11]. More often, the mixed Cu–Co oxide catalysts reported in these studies were thin films or coatings fabricated through magnetron sputtering [6,50] or binder less-electrodes on substrates produced via hydrothermal synthesis [51]. As such, there have been very minimal accounts on the application of powder catalysts in literature [52]. The usage of this form of the catalyst offers easier fabrication of the MEA and ensures that the amount of electrode material is sufficient for

practical electrolyzer operations [52]. Furthermore, the application of hierarchically structured, powdered $Cu_xCo_{3-x}O_4$ catalyst in AAEMWE has not been explored yet to the best of our knowledge.

In this report, hierarchical urchin-like, spinel $Cu_xCo_{3-x}O_4$ was synthesized using an ethanol-assisted hydrothermal route and tested for OER catalysis. Subsequently, the effect of the Cu-dopant concentration on the morphology, structure, and catalytic activity of the Co_3O_4 catalyst was investigated. Finally, the performance of the best $Cu_xCo_{3-x}O_4$ catalyst in an AAEMWE was evaluated at varying operating temperatures.

2. Materials and methods

2.1. Ethanol-assisted hydrothermal synthesis of the $Cu_xCo_{3-x}O_4$ electrocatalysts

In this study, the activity of $Cu_xCo_{3-x}O_4$ (Cu-doped Co_3O_4) electrocatalysts towards OER is studied. As previously discussed, Co_3O_4, as a base material, already exhibits high OER activity and excellent stability in alkaline environments. Introducing dopants into the Co_3O_4 structure increases its conductivity, which in effect also increases its efficiency as an OER catalyst. Herein, Cu was used as the dopant owing to its abundance, good conductivity, and cost-effectiveness,[53] which is a crucial criterion for practical application.

$Cu_xCo_{3-x}O_4$ samples were synthesized through an ethanol-assisted hydrothermal method. All of the chemical reagents used herein were of analytical grade and did not undergo further purification. In a typical procedure, 2 g of CH_4N_2O (Techno Pharmchem, 99.5%) was added into a 30 mL solution (1:2) of anhydrous C_2H_5OH (Ajax Finechem, 100%) and distilled water. Then, a total of 5 mmol of $Co(NO_3)_2 \cdot 6\ H_2O$ (Sigma-Aldrich, 98%) and $Cu(NO_3)_2 \cdot 2.5\ H_2O$ (Sigma-Aldrich, 98%) were mixed accordingly to prepare five compositions of $Cu_xCo_{3-x}O_4$ (x = 0, 0.25, 0.5, 0.75, and 1). After stirring the resulting solution for 30 min, 0.5 g cetyltrimethylammonium bromide (CTAB, $C_{19}H_{42}BrN$, Loba Chemie, 99%) was added. To

ensure homogeneous mixing, the solutions were stirred at 300 rpm for another 30 min, and then transferred into 100 mL Teflon-lined steel autoclaves. The hydrothermal reaction was done at 100 °C for 10 h. Afterward, the precipitates were collected via centrifugation, washed three times with distilled H_2O and absolute ethanol, and then dried at 70 °C for 2 h. Finally, the powders were calcined at 400 °C for 6 h with a heating rate of 1 °C min^{-1} from room temperature.

2.2. Material characterization

The samples used for all the subsequent material characterization and electrochemical tests were obtained after the calcination of the hydrothermal reaction products unless specified otherwise. The morphologies of the synthesized $Cu_xCo_{3-x}O_4$ electrocatalysts were observed through field emission scanning electron microscopy (FE-SEM, Hitachi SU 8230). Structural analyses and phase identification were done through X-ray diffraction measurements on a PanAlytical X'pert PRO MPD diffractometer with Cu-Kα radiation, $\lambda = 0.15406$ nm. Rietveld refinement was done afterwards to identify the phase composition of the samples. The cation distributions of the $Cu_xCo_{3-x}O_4$ products were estimated from quantitative XRD measurements through the best-fit equation [54]:

$$a = 2.0995\alpha + (5.8182\beta^2 - 1.4107\alpha^2)^{\frac{1}{2}}$$

Therein,

$$\alpha = \frac{\sum x_i(M_i - O)_{T_d}}{\sum x_i}$$

and

$$\beta = \frac{\sum x_i(M_i - O)_{O_h}}{\sum x_i}$$

where x_i is the stoichiometric coefficient of the cation M_i, and $(M_i - O)$ is the distance of M_i with oxygen in the tetrahedral (T_d) and octahedral (O_h) sites [11,39]. Specific surface areas (SSA) of the samples were determined through Brunauer–Emmett–Teller (BET) method from N_2 adsorption measurements at 77.35 K using Quantochrome Nova Station B.

2.3. Electrochemical measurements

Electrochemical measurements were done in a three-electrode cell setup using MetroOhm Autolab® potentiostat PGSTAT10. The reference and counter electrodes used are Ag/AgCl (silver/silver chloride, 3.3 M KCl, Metrohm), and platinum (Pt) wire, respectively. All potentials were converted against the reversible hydrogen electrode (RHE). The working electrode was prepared by depositing 90 µL of the catalyst ink, which is a suspension of 10 mg catalyst in 2 mL ethanol with 20 µL 5% (wt/wt) polyvinylidene fluoride binder (($C_2H_2F_2$)$_n$, M_w = 10000), onto carbon fiber paper (CFP) substrates. The geometrical area of the working electrode is about 0.785 cm^2, while the effective mass loading was 0.2 mg cm^{-2}.

Before OER activity testing, 1.52 V (*vs. RHE*) was applied onto the working electrode for 30 min. Electrochemical impedance spectroscopy (EIS) at 1.72 V (*vs. RHE*) with frequency ranging from 10 kHz to 0.1 Hz and an amplitude of 30 mV was done before and after the initial chronoamperometric hold. Then, cyclic voltammetry from 1.22 to 1.57 V (*vs.* RHE) was performed for 10 cycles at a scan rate of 5 mV s^{-1}. OER polarization curves were then obtained through linear sweep voltammetry (LSV) from 1.2 to 1.8 V (*vs. RHE*) at a scan rate of 1 mV s^{-1} for 5 scans to obtain stable performance. The electrochemical active surface area of the samples was estimated through cyclic voltammetry scans at the non-Faradaic region (1 to 1.3 V (*vs. RHE*) recorded at 10, 20, 30, 40, and 50 mV s^{-1}. The double-layer capacitance was calculated from the slope of the linear regression curve of the capacitive current against scan rate plot. ECSA was calculated by dividing the obtained C_{dl} values by the specific capacitance

for ideal, flat surfaces ($C_s \approx 40$ μm cm^{-2}) [43]. Stability tests were conducted by subjecting the working electrode to 2000 cycles of polarization from 1.22 to 1.57 V (*vs.* Ag/AgCl) at a scan rate of 100 mV s^{-1}. All experiments were done at room temperature and ambient pressure using 1 M KOH electrolyte.

2.4. Electrolyzer measurements

Electrolyzer measurements were done using a titanium cell body with gold coated serpentine flow fields with an active area of 1 cm^2 (Scheme 1). Cell temperature control was done using thermostatically controlled cartridge heaters put into the cell body. The anode was prepared by spraying the $Cu_xCo_{3-x}O_4$ catalyst dispersed in 12.5 wt% SEBS ionomer [55,56] and n-methyl-2-pyrrolidone, on a 300 μm Ti fiber felt gas diffusion layer (GDL) (Bekaert S.A., Fibre Technologies) with 78% porosity. Catalyst loading at the anode was 2 mg cm^{-2}. On the other hand, the cathode was prepared by spraying a mixture of 20% Pt/C, 28 wt% SEBS ionomer, and isopropanol onto a non-wet proof carbon GDL (Freudenberg Germany). The effective loading was 0.4 mg cm^{-2}. LDPE–VBC–TMA-based AAEM was used. The MEA was made by sandwiching the anode and cathode either side of the membrane. Electrolyzer testing was conducted using a Gamry potentiostat (IFC 5000E) in 1 M KOH electrolyte solution at 20 and 60 °C.
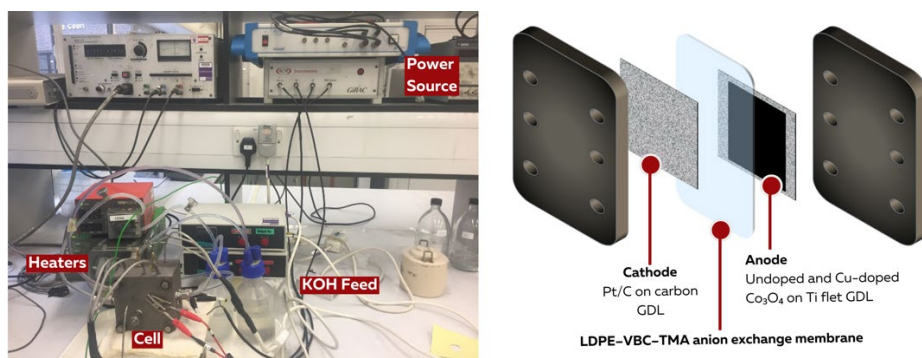
Scheme 1. Full cell testing setup and membrane electrode assembly used in the study.

3. Results and discussion
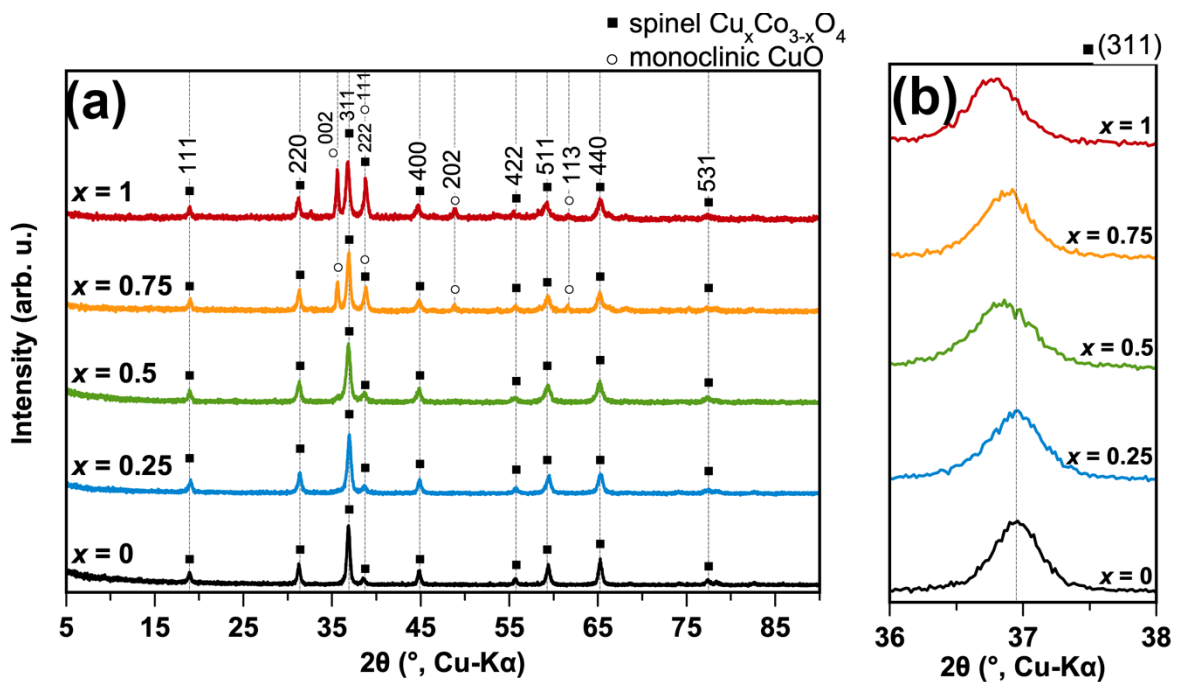
3.1. Crystal structure and morphology of the products

Figure 1. (a) XRD patterns of the $Cu_xCo_{3-x}O_4$ products with varying dopant concentration x, and (b) magnified image of the 311 peaks.

Fig. 1(a) shows the XRD patterns of the $Cu_xCo_{3-x}O_4$ products with varying Cu-doping concentrations at x = 0, 0.25, 0.5, 0.75, and 1. The peaks at 2θ = 18.90°, 31.24°, 36.86°, 38.66°, 44.90°, 55.78°, 59.38°, 65.26°, and 77.40°, which are observed at the XRD pattern of the undoped sample (x = 0), corresponds well to the 111, 220, 311, 222, 400, 422, 511, 440, and 531 planes of the cubic spinel Co_3O_4 lattice (JCPDS-PDF # 42-1467) [57]. On the other hand, the diffraction patterns of the products obtained with Cu-doping at x = 0.25 and 0.5 are similar to that of the undoped sample. No other peaks were observed, indicating that the introduction of Cu^{2+} into the spinel Co_3O_4 lattice did not result in the formation of a secondary phase [47,49].

As the amount of Cu was increased to achieve doping at x = 0.75 and 1, a slight phase separation to CuO occurred. The peaks at 2θ = 35.74°, 48.82°, and 61.66°, which could be indexed to 002,

10

202, and 113 peaks of monoclinic CuO (JCPDS-PDF # 01-089-5895), became apparent [58].

Additionally, the peak at $2\theta = 38.66°$, which was previously indexed to 222 peak of the parental

spinel only, showed an increase in intensity. This could also be due to the emergence of a CuO

phase because this peak also corresponds to the 111 plane of the monoclinic lattice [59]. Rietveld

analysis, shown in Fig. S1, revealed that the products synthesized with Cu-doping at $x = 0.75$

and 1 both contained 24.5 and 64.0 wt% CuO, respectively. These findings agree well with

previous reports that a solid solution of $Cu_xCo_{3-x}O_4$ may form from the incorporation of Cu^{2+}

ions into spinel Co_3O_4 at intermediate values of x, and more commonly, when x < 1 [11,39,47,60,61].

From the magnified image of the XRD pattern from $2\theta = 36°$ to $38°$ shown in Fig. 1(b), the

broadening of the 311 peaks of $Cu_xCo_{3-x}O_4$ was apparent. From this, it can be deduced that the

incorporation of Cu^{2+} resulted in a reduction in the crystallinity of the spinel lattice [62]. This

finding can also be supported by the larger full width at half maximum (FWHM) values of the

311 peaks recorded for Cu-doped samples in contrast to that of the undoped Co_3O_4, which are

listed in Table 1. Correspondingly, the crystallite sizes calculated from these FWHM values

decreased as the parental Co_3O_4 spinel was doped with Cu^{2+} ions. Larger ions induce strain

when they substitute ions in the lattice. As the concentration of these bigger ions increases as

a result of higher dopant concentration, the strain induced in the lattice is intensified. This,

however, can be minimized through the accommodation of the dopants on the grain or the

crystallite surface. With this, the surface area-to-volume ratio increases, and the crystallite size

decreases due to the segregation of the dopants on the surface. Therefore, as a consequence of

doping, the crystallite size is reduced to minimize the energy and the strain of the lattice [40].

Table 1. Full width at half maximum values of the 311 peaks of $Cu_xCo_{3-x}O_4$, and lattice parametrs after Rietveld refinement; calculated crystallite size, y value, and cation distribution of the $Cu_xCo_{3-x}O_4$ products

x value	FWHM [°]	Crystallite Size [nm]	a_0 [Å]	y value	Cation Distribution
0	0.406	20.650	8.086	-	$(Co_1^{2+})_{Td}(Co_2^{3+})_{Oh}O_4$
0.25	0.532	18.144	8.098	0.10	$(Co_{0.75}^{2+}Cu_{0.15}^{2+}Co_{0.10}^{3+})_{Td}(Co_{1.90}^{3+}Cu_{0.10}^{2+})_{Oh}O_4$
0.50	0.626	13.364	8.098	0.13	$(Co_{0.50}^{2+}Cu_{0.37}^{2+}Co_{0.13}^{3+})_{Td}(Co_{1.87}^{3+}Cu_{0.13}^{2+})_{Oh}O_4$
0.75	0.506	13.694	8.098	0.17	$(Co_{0.25}^{2+}Cu_{0.57}^{2+}Co_{0.17}^{3+})_{Td}(Co_{1.83}^{3+}Cu_{0.17}^{2+})_{Oh}O_4$
1	0.577	13.771	8.093	0.15	$(Cu_{0.85}^{2+}Co_{0.15}^{3+})_{Td}(Co_{1.85}^{3+}Cu_{0.15}^{2+})_{Oh}O_4$

Table 1 also shows the lattice parameters, which are obtained after Rietveld refinement, the y values, which tell the amount of Cu in O_h sites, and the corresponding cation distributions of the samples. The unit cell parameter recorded for the undoped product agrees well with that of spinel Co_3O_4 (8.084 Å) [62,63]. Enlargement of the lattice was observed, as the cell parameter increased with Cu-doping. This can be explained by the arrangement of the ions forming the spinel lattice. Co_3O_4 spinel structure is formed by Co^{2+} and Co^{3+} ions, which are situated at the interstitial tetrahedral (T_d), and octahedral sites (O_h) of a face-centered cubic (FCC) lattice of oxygen atoms [64]. In a normal transition metal-doped Co_3O_4 spinel, the transition metal cation substitutes a Co^{2+} ion in a tetrahedral location [11]. However, for $Cu_xCo_{3-x}O_4$, lattice inversion occurs when $x > 0.2$, that is, the normal spinel transitions to an inverse structure: $Co_{1-x}^{2+}Cu_{x-y}^{2+}Co_y^{3+}[Co_{2-y}^{3+}Cu_y^{2+}]O_4$, where some Cu^{2+} ions occupy O_h sites causing some Co^{3+} ions to sit into tetrahedral T_d sites [11,39,65,66]. In this structure, y is the amount of Cu in the O_h sites; hence, it is the measure of the degree of inversion of the spinel structure. In Table 1, it can be seen that the y value increases with x. That is to say, that, as more Cu dopants are introduced, more Cu^{2+} ions hold O_h sites, and more Co^{3+} ions are displaced into T_d sites.

Accordingly, as can be seen in Fig. 1(b), the 311 peak position shifted to a lower 2θ value as more Cu^{2+} was introduced. This further confirms the inversion between $Cu_{T_d}^{2+}$ and $Co_{O_h}^{3+}$ because it denotes that Cu-dopant species also occupy interstitial O_h sites, in addition to substitution lattice sites [39,67]. The ionic radii of Co ions are 58 and 52.5 pm in the T_d, and O_h sites, respectively. On the contrary, those of the Cu ions are 57 and 73 pm [68,69]. Therefore, the expansion of the Co_3O_4 crystal lattice occurred due to the inversion, and the substitution of the smaller cobalt cations in the O_h sites with the larger Cu cations [11,57].
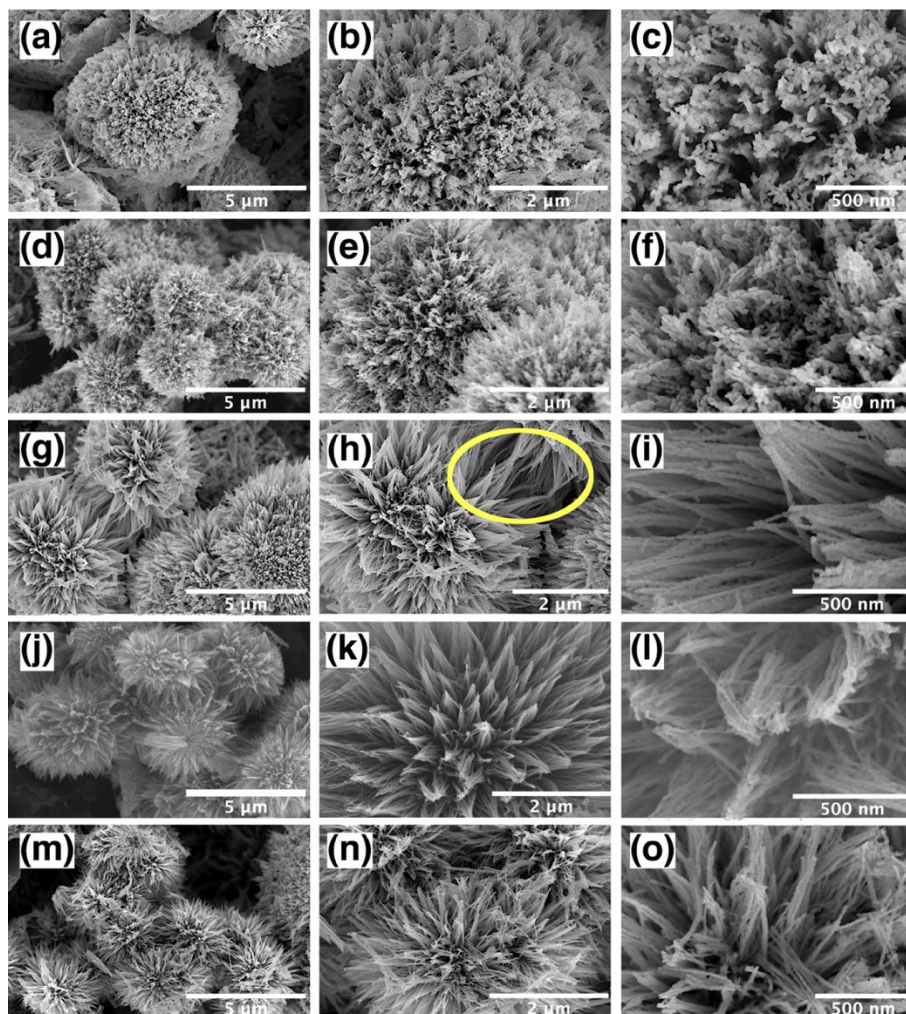
Figure 2. FESEM images of the synthesized $Cu_xCo_{3-x}O_4$ spinels: $x = 0$ (a-c), 0.25 (d-f), 0.50 (g-i), 0.75 (j-l) and 1 (m-o). [Encircled: Interconnections of the urchin-like particles observed at $x = 0.5$]

Fig. 2 shows the FESEM images of the synthesized $Cu_xCo_{3-x}O_4$ spinels. Fig. 2(a) reveals the urchin-like morphology of the undopd Co_3O_4. The urchin-like Co_3O_4 microspheres, with an average diameter of 5.69 ± 1.54 μm, are composed of highly dense nanowires [70]. These one-dimensional nanostructures grew outward from a common center, and are subsequently formed by interconnected, irregularly shaped nanoparticles [Fig. 2(b)–(c)] [71]. As Cu was introduced, the as-synthesized spinel retained their urchin-like morphology. At $x = 0.25$, the microspheres are about 3.79 μm (SD = 0.907) in diameter [Fig. 2(d)–(e)]. Further inspection reveals that the nanowires forming the urchin-like structure are still composed of connected nanoparticles [Fig. 2(f)]. The urchin microspheres produced with Cu-doping at $x = 0.5$ [Fig. 2(g)–(h)], $x = 0.75$ [Fig. 2(j)–(k)], and $x = 1$ [Fig. 2(m)–(n)] have average diameters of 5.91 μm (SD = 0.489), 4.08 μm (SD = 0.404), and 3.37 μm (SD = 0.484), respectively. As encircled in Fig. 2(h), the urchins are also more interconnected, which may be beneficial in the catalytic activity of the spinel because it can facilitate electron and ion transfer processes more efficiently. Furthermore, the nanowires forming such structures are visibly finer and thinner [Fig. 2(i), (l) & (o)]. Apart from the urchin-like microspheres, nanosheets were also formed with Cu doping at $x = 0.75$ and 1. Sheet-like structures, shown in Fig. S2, were observed possibly due to the emergence of a secondary CuO phase [49].

Table 2. Microstructural properties of the $Cu_xCo_{3-x}O_4$ products obtained by BET and analyses of N_2 adsorption isotherms shown in Fig. S3

x value	BET Surface Area [m^2 g^{-1}]
0	29.235
0.25	35.326
0.5	36.119
0.75	40.937
1	37.557

Fig. S3 shows the N_2 adsorption isotherms of $Cu_xCo_{3-x}O_4$ products in the logarithmic pressure scale at low relative pressures. Type II adsorption isotherms were recorded, which indicates that the samples are either non-porous or microporous [72]. The surface microstructural properties, which are obtained from surface area measurements, of the $Cu_xCo_{3-x}O_4$ products are listed in Table 2. Specific BET surface area continued to increase from 29.235 to 40.937 m^2g^{-1} as Co_3O_4 was doped until $x = 0.75$. This agrees well with the decreasing crystallite size values calculated from the XRD results, which indicate that the surface area-to-volume ratio needs to increase to minimize the lattice strain induced by the introduction of the dopant Cu^{2+} ions [40].

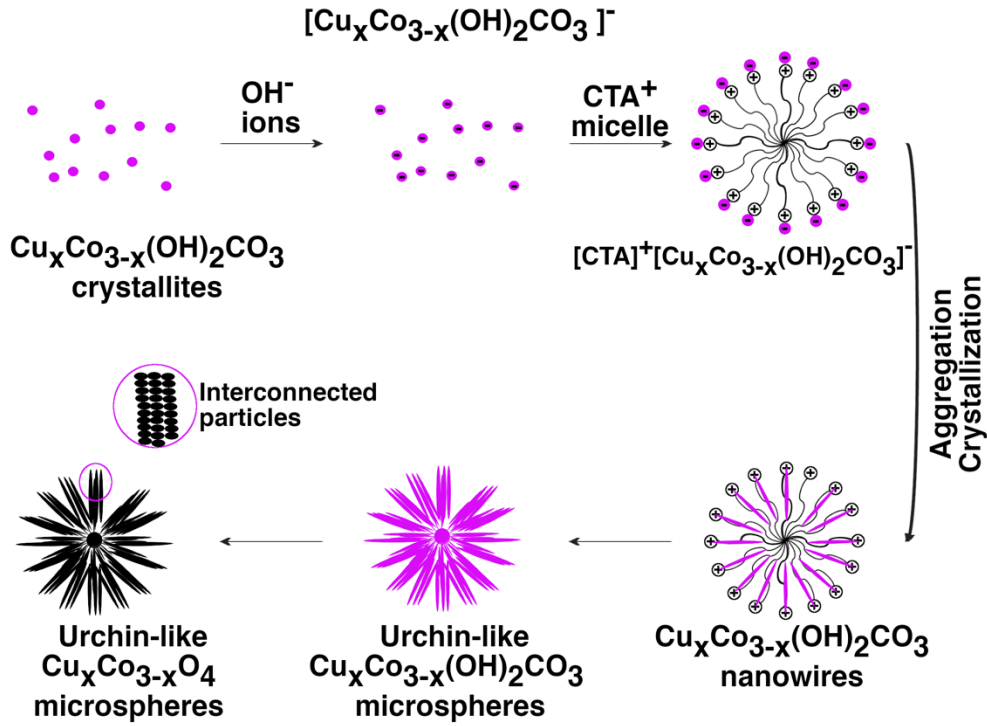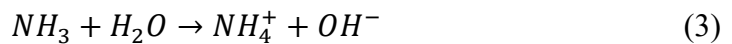## 3.2. Formation mechanism of $Cu_xCo_{3-x}O_4$ urchin-like microspheres

Figure 3. Proposed mechanism for the formation of the urchin-like $Cu_xCo_{3-x}O_4$ microspheres

Fig. 3 shows the proposed formation mechanism of the urchin-like $Cu_xCo_{3-x}O_4$ microspheres. In this study, urea was used as a precipitating agent. In an aqueous solution, it slowly disassociates into carbonate, and hydroxide ions according to Eq. (1) to (3) [73,74].

$$CO(NH_2)_2 + H_2O \rightarrow 2\,NH_3 + CO_2 \tag{1}$$

$$CO_2 + H_2O \rightarrow CO_3^{2-} + 2\,H^+ \tag{2}$$

$$NH_3 + H_2O \rightarrow NH_4^+ + OH^- \tag{3}$$
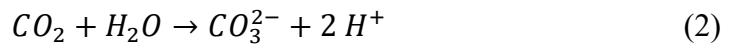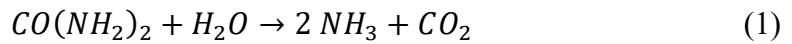
The produced OH^- and CO_3^{2-} anions react with the Co^{2+} and Cu^{2+} cations in the solution [75]. According to Eq. (4), this reaction forms Co and Cu-Co metal hydroxide carbonates with and without Cu-doping, respectively [73].

$$(3 - x)\, Co^{2+} + x\, Cu^{2+} + 2\, OH^- + CO_3^{2-} \rightarrow Cu_x Co_{3-x}(OH)_2 CO_3 \qquad (4)$$
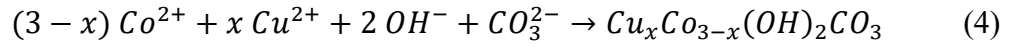
Initially, these metal hydroxide carbonate crystallites (MHCC) are formed. Excessive OH^- ions in the solution are then adsorbed on the surface of the MHCC, thereby forming the $Cu_xCo_{3-x}(OH)_2CO_3 \cdot OH^-$ precursor [73]. This precursor carried net negative surface charge, which hinders aggregation due to the presence of a strong repulsive force between the nuclei. Through the addition of the cationic surfactant, CTAB, the zeta potential is reduced by the electrostatic interaction between CTA^+ formed in the aqueous solution, and $Cu_xCo_{3-x}(OH)_2CO_3 \cdot OH^-$ [76]. This interaction produced CTA^+-$Cu_xCo_{3-x}(OH)_2CO_3 \cdot OH^-$ ion pairs, with the initially produced $Cu_xCo_{2-x}(OH)_2CO_3 \cdot OH^-$ crystallites oriented perpendicular to the microsphere surface and pointed towards the center of the CTA^+ micelles [73]. The repulsive force between the particles was then decreased, thus promoting aggregation, crystallization, and formation of nanowire-like structures. The XRD patterns of the uncalcined undoped ($x = 0$) and Cu-doped ($x = 0.75$) powders, which are shown in Fig. S4(a), confirm the syntheses of the MHC precursors. For the undoped precursor, the reflection peaks at $2\theta = 17.46°$, $33.80°$ and $35.08°$ correspond to the 020, 221, and 040 planes of $Co_2CO_3(OH_2)$, respectively (JCPDS-PDF # 48-0083) [77]. On the other hand, all the reflection peaks are well-indexed to $(Cu,Co)_2CO_3(OH_2)$ with Cu-doping at $x = 0.75$ (JCPDS-PDF # 0029-1416) [77,78].

Fig. S4 (b, c) shows the FESEM images of the uncalcined powder obtained with Cu-doping at $x = 0.75$. Prior to calcination, it can be seen that the $(Cu,Co)_2CO_3(OH_2)$ precursor exhibits an urchin-like morphology, which is composed of smooth nanowires. According to Eq. (5), CO_2 and H_2O gases, as well as surfactant residues, are released during calcination. This makes the surface of the nanowire rough; hence the formation of interconnected structures of irregularly shaped nanoparticles observed in the $Cu_xCo_{3-x}O_4$ spinels [43,75].

$$Cu_xCo_{3-x}(OH)_2CO_3 + \frac{7}{2}O_2 \xrightarrow{\Delta} Cu_xCo_{3-x}O_4 + H_2O + CO_2 \qquad (5)$$
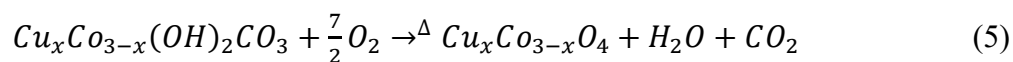
As previously discussed, the nanowires, which formed the urchin-like microspheres with Cu-doping at $x = 0.5$, 0.75, and 1, became finer. This is consistent with the decreasing crystallite sizes obtained with increasing amounts of Cu^{2+} as determined through XRD analysis. Moreover, this finding denotes that higher Cu concentrations restrained the growth of Co_3O_4 due to the smaller Pauling electronegativity of Cu over Co. As Co is more reactive, the growth rate of Co_3O_4 is decreased upon the incorporation of Cu^{2+}, thereby forming thinner nanowires [67].

3.3. Electrochemical oxygen evolution studies on the urchin-like $Cu_xCo_{3-x}O_4$ catalysts

For the ease of discussion, $Cu_xCo_{3-x}O_4$: $x = 0$, 0.25, 0.5, 0.75 and 1 will be referred to as CCO-0, 0.25, 0.5, 0.75, and 1, respectively, from this point of the article onwards. Before the recording of the linear sweep voltammograms, all samples were subjected to a 30 min-chronoamperometric hold at 1.52 V (*vs. RHE*) to obtain more stable electrochemical responses. Fig. S5(a) shows the chronoamperometric plots of the samples. It can be seen that throughout the stabilization step, all samples registered stable constant current densities with very minute fluctuations. To understand the effect of the stabilization step better, the impedance spectra of the samples before and after the chronoamperometric hold are shown in Fig. S5(b) – (f). The equivalent circuit shown in Fig. S6 was used in fitting the obtained impedance spectra. Slight shifts were observed for all impedance spectra after the stabilization step. The high-frequency intercepts, which are indicative of the ohmic resistances, increased by 0.09 Ω cm^2 for both CCO-0 and CCO-0.25; 0.18 Ω cm^2 for CCO-0.5; and 0.06 Ω cm^2 for CCO-0.75 and CCO-1. Moreover, the area-specific charge transfer resistance (R_{ct}) obtained from the difference between the high- and low-frequency intercepts along the Z' axis also increased for all samples.

18

The largest impedance spectra shift (0.21 Ω cm^2) was recorded for CCO-0. On the other hand, R_{ct} was about 0.13 Ω cm^2 for CCO-0.25 and CCO-0.5; 0.16 Ω cm^2 for CCO-0.75; and 0.12 Ω cm^2 for CCO-1. The observed shifts on the electrochemical impedance spectra of the samples suggest the possible increase of the average oxidation state of Co after the chronoamperometric hold; that is, its oxidation from Co^{3+} to Co^{4+} [79]. These shifts also explain the very minute reductions in the current densities registered during the 30 min stabilization step.
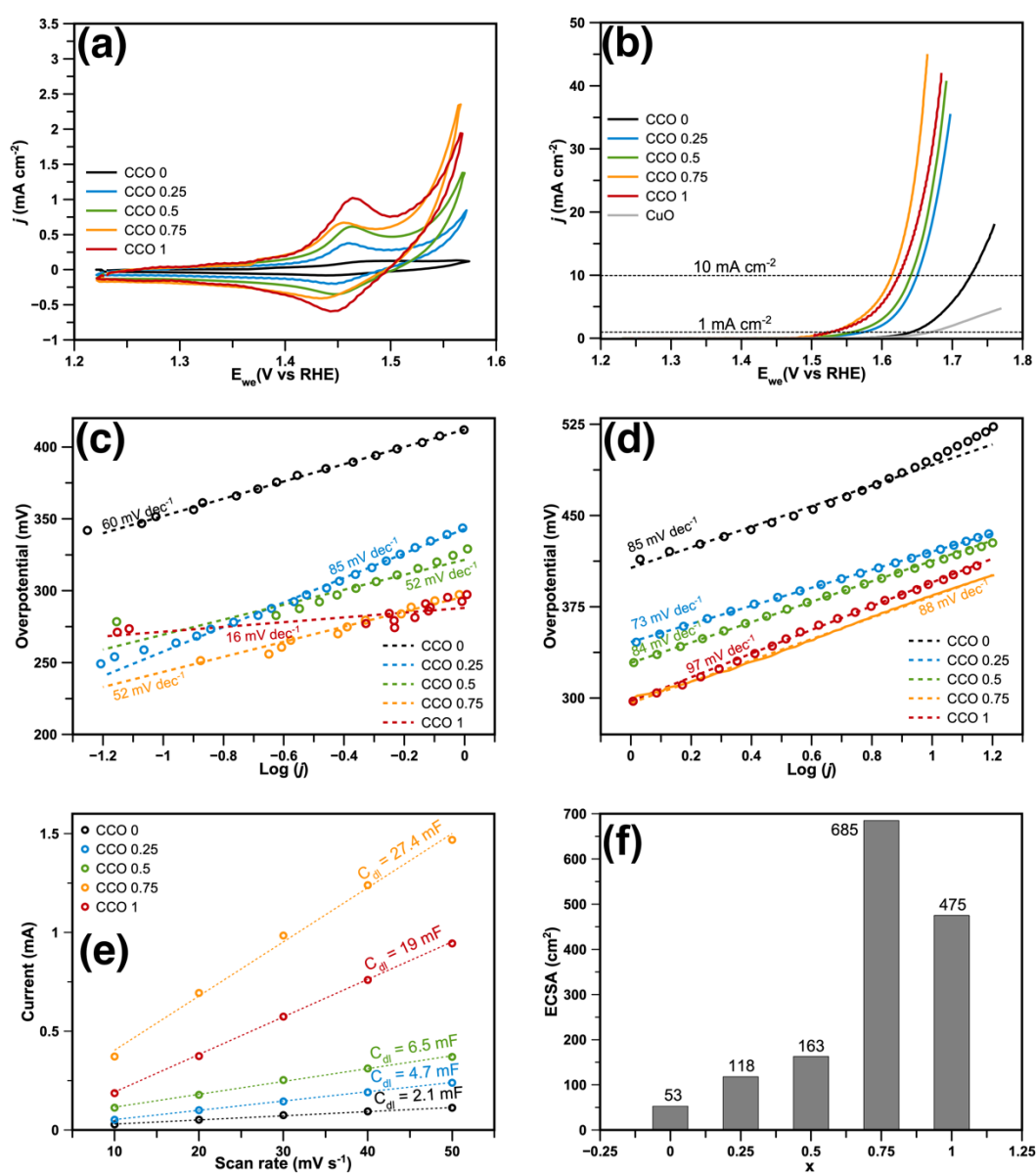
Figure 4. *i*R-corrected (a) cyclic voltammograms from 1.22 to 1.57 V (*vs. RHE*), (b) linear sweep voltammograms from 1.20 to 1.80 V (*vs. RHE*) obtained at 1 mV s^{-1} in 1 M KOH electrolyte, and Tafel plots at the (c) low and (d) high current density regions, (e) double-layer capacitance, and (f) electrochemical active surface area (ECSA) of the samples

Fig. 4(a) shows the *i*R-corrected cyclic voltammograms from 1.22 to 1.57 V (*vs. RHE*) of the $Cu_xCo_{3-x}O_4$ catalysts in 1 M KOH. Table 3 summarizes the electrochemical parameters obtained from the three-electrode setup testing. During the initial stages of the anodic scan, the surface of the undoped Co_3O_4 electrode is hydrated (Eq. 6), and then oxidized further upon the application of higher potentials (Eq. 7) [62].

$$Co_3O_4 + H_2O + OH^- \rightarrow 3\,Co - OOH + e^- \qquad (6)$$

$$Co - OOH + OH^- \rightarrow Co - O_2 + e^- + H_2O \qquad (7)$$
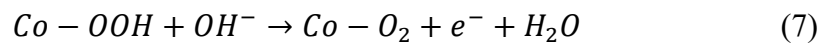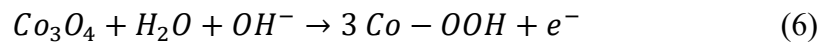
The anodic peak around 1.45 to 1.50 V (*vs. RHE*), which corresponds to the oxidation of Co^{3+} to Co^{4+} as in Eq. (7), was not defined in the voltammogram of the undoped Co_3O_4 catalyst, as seen in Fig. 4(a). Upon the incorporation of Cu^{2+} ions into Co_3O_4, this oxidation peak became notable. The anodic peak potential (E_{pa}) was about 1.46 V (*vs. RHE*) for all the samples, with CCO-0.75 registering the most negative E_{pa} of 1.455 V (*vs. RHE*). There are limited reports in literature that explain the shifting of the anodic peak towards less positive potentials due to Cu-doping. From previous observations, the shifting of the anodic peak towards less positive potentials may be due to the interaction between different factors. First, lattice inversion was observed as a consequence of Cu-doping. As previously discussed, at *x* values > 0.2, Co^{3+} ions, which are previously situated in O_h sites of the spinel lattice, migrate to the T_d locations to accommodate the incoming Cu^{2+} ions. This inversion altered the surface structure and properties, which possibly brought about the change in recorded E_{pa} values [11,80]. Second, with increasing Cu^{2+} concentration, the anodic peak visibly became more defined, and the peak

20

height increased. Peak intensity is known to vary in direct proportion with the electrochemically active surface area. Therefore, more active sites are made available for the redox reaction as Cu^{2+} concentration was increased [62,81]. The highest peak height was recorded on the CCO-1 electrode, which suggests favorable reaction kinetics before OER. Moreover, the recorded current potentials of the Cu-doped Co_3O_4 catalysts at the end of the potential window were significantly larger than that of pure Co_3O_4. Case in point, the current density of CCO-0.75 and CCO-1 at 1.57 V (*vs. RHE*) were about 20 and 16 times that of the CCO-0, respectively.

Fig. 4(b) shows the *i*R-corrected linear sweep voltammograms of the $Cu_xCo_{3-x}O_4$ catalysts at a scan rate of 1 mVs^{-1} in 1 M KOH. After the reaction in Eq. (7), oxygen evolution commences as the Co–O_2 bond is severed due to the application of increasing potential. The onset potential recorded at 1 mA cm^{-2} for the undoped Co_3O_4 electrode was 1.701 V, which corresponds to an overpotential of 417 mV. As Cu^{2+} was introduced to the Co_3O_4 catalyst, the overpotential at 1 mA cm^{-2} continued to decrease to as low as 297 mV with increasing dopant concentration. This was recorded for CCO-1. At low current densities, Cu-doping at $x = 1$ resulted in the best electrocatalytic activity as supported by the lowest onset overpotential observed, as well as the highest anodic peak height attained as previously discussed. These results show that Cu-incorporation led to the enhancement of the OER catalytic activity of spinel Co_3O_4. After the introduction of Cu^{2+} ions, the crystallite sizes of the doped catalysts were lower than that of the undoped Co_3O_4. Even more, the nanowires forming the micro urchin-like structures became thinner. These two factors led to the increase in the specific surface areas of the catalysts as evidenced by the increasing BET measurements. Therefore, the observed enhancement in the OER activity is possibly due to the higher specific surface area, which provides more active sites for the reaction and promotes faster reaction kinetics as a result of the more rapid transport of ions in the electrolyte [43,62,82]. The faster reaction kinetics in the low current density region

can also be seen in the reduction of the Tafel slopes as shown in Fig. 4(c) [83]. CCO-1 registered a Tafel slope of 16 mV dec^{-1}, which is drastically smaller than that of CCO-0 (60 mV dec^{-1}). As shown in Table 3, the reduction in the R_{ct} values from 7.92 Ω cm^2 to as low as 1.69 Ω cm^2 proves further the enhancement in the catalytic kinetics of the catalysts and indicates the facilitation of charge-transfer processes after Cu-doping [82–84].

On the other hand, at higher current densities, CCO-0.75 exhibited the most pronounced catalytic activity enhancement. At 10 mA cm^{-2}, the overpotential gradually declined from 509 to 385 mV as the catalyst was doped with Cu^{2+} until $x = 0.75$. Beyond $x = 0.75$, the overpotential recorded increased to 394 mV. Even more, the current density achieved at 1.6 V (*vs. RHE*) increased in the order: x = 0 (1.93 mA cm^{-2}) $< x = 0.25$ (13.77 mA cm^{-2}) $< x = 0.5$ (17.22 mA cm^{-2}) $< x = 1$ (23.18 mA cm^{-2}) $< x = 0.75$ (39.30 mA cm^{-2}). These indicate that at the high j region, CCO-0.75 outperformed CCO-1. Relative to the undoped CCO-0 catalyst, the catalytic activity of the samples improved with Cu-doping at $x = 1$. However, the enhancement was offset beyond $x = 0.75$ because of the increase in the amount of the resistive secondary CuO phase formed. To illustrate the effect of CuO on the electrocatalytic activity of CCO-0.75 and 1, pure CuO was synthesized through the same ethanol-assisted hydrothermal method and was subsequently tested for OER catalysis. From the LSV graph of CuO shown in Fig. 4 (b), it can be seen that CuO exhibited very poor activity towards OER catalysis. It recorded an onset overpotential as high as 412 mV, which is about 37% more than those of CCO-0.75 and 1. From the Nyquist plot shown in Fig. S7(a), the R_{ct} of CuO was found to be 24.5 Ω cm^2, which is about three and fifteen times that of CCO-0 and CCO-0.75, respectively. The highly resistive nature of CuO is also reflected in the calculated Tafel slope, which is about 160 mV dec^{-1} [Fig. S7(b)]. The high ionic resistance of CuO drastically affected the kinetics of the electrochemical reactions during OER activity testing. This effect was more pronounced for CCO-1 because it contains about 64% CuO, and probably caused the increase in the calculated Tafel slope to 97

mV dec^{-1} [Fig. 4(d)]. At high j regions, an increase in the coverage of the reaction intermediates can be observed in the catalyst surfaces. Therefore, the effect of the CuO phase became more pronounced in this region possibly because the high resistance it imparts to the catalyst prevents the efficient adsorption and desorption of these reaction intermediates, which are required for favorable OER electrocatalysis [79]. The superior electrochemical performance of CCO-0.75 can also be attributed to its high specific surface area and huge electrochemical surface area. From the current measured at 1.25 V (vs. Ag/AgCl) vs. scan rate plots in Fig. 4(e), the double-layer capacitance (C_{dl}) of the samples was calculated. Thereafter, the ECSA of the electrocatalysts, which are shown in Fig. 4(f), were calculated by dividing C_{dl} by the theoretical value of specific capacitance for flat surfaces ($C_s \sim 40 \ \mu F \ cm^{-2}$) [43,85]. From Fig. 4(f), it can be seen that the ECSA increased as the sample was doped until $x = 0.75$ from 53 to 685 cm^2, and then, decreased as doping was done with $x = 1$. This finding shows that the electrochemical reactions occurred most favorably on the surface of CCO-0.75 electrode. The increase in the ECSA is in accordance with the XRD findings, which indicate that the surface area-to-volume ratio needs to increase to minimize the lattice strain induced by the introduction of the dopant Cu^{2+} ions [40]. ECSA possibly declined beyond $x = 0.75$ (for CCO-1) because of the formation of more CuO nanosheets, which contributes less surface area than the hierarchical urchin-like structures [49].

Table 3. Anodic peak potentials, overpotentials at onset (1 mA cm^{-2}), and 10 mA cm^{-2}; Tafel slopes in the low and high current density regions; and charge transfer resistances of the Cu$_x$Co$_{3-x}$O$_4$ electrodes

x	E_{pa} [V]	η_{onset} [mV]	η_{10} [mV]	Tafel Slope at low j [mV dec^{-1}]	Tafel Slope at high j [mV dec^{-1}]	R_{ct} [Ω cm^2]
0	-	417	509	60	85	7.92
0.25	1.462	345	420	85	73	1.55
0.5	1.463	329	412	52	84	1.81
0.75	1.455	299	385	52	88	1.84
1	1.463	297	394	16	97	2.04
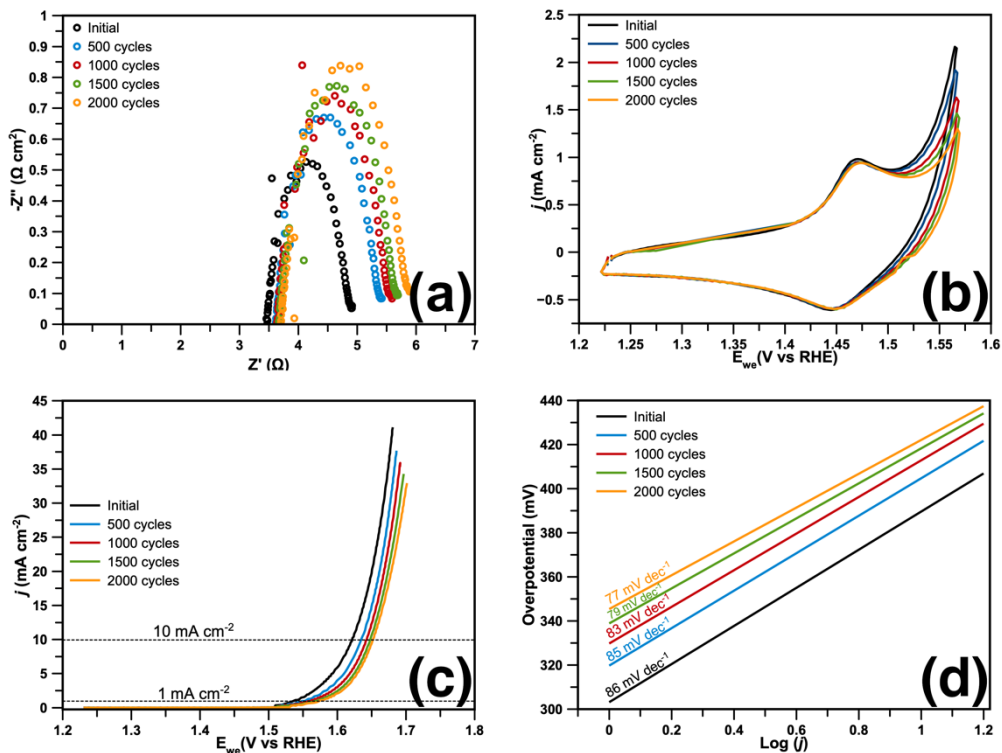
Figure 5. (a) Nyquist plots, *i*R-corrected (b) cyclic voltammograms from 1.22 to 1.57 V (*vs. RHE*), and (c) linear sweep voltammograms from 1.20 to 1.80 V (*vs. RHE*) obtained at 1 mVs^{-1}; and (d) Tafel plots at the high current density regions of CCO-0.75 before and after stability test in 1 M KOH electrolyte

Table 4. Key electrochemical parameters observed for CCO-0.75 before and after 500, 1000, 1500, and 2000 cycles of application of 1.22 to 1.57 V (*vs. RHE*) at 100 mV s^{-1} in 1 M KOH electrolyte

Cycle	R_{ct} [Ω cm^2]	E_{pa} [V]	η_{onset} [mV]	η_{10} [mV]	Tafel Slope at high j [mV dec^{-1}]
0	1.44	1.471	299	385	88
500	1.88	1.471	322	405	85
1000	1.95	1.471	333	413	83
1500	2.02	1.474	340	418	79

2000	2.20	1.474	345	422	77

Fig. 5 shows the electrochemical response of CCO-0.75 before and after 500, 1000, 1500, and 2000 cycles of application of 1.22 to 1.57 V (*vs. RHE*) at 100 mV s^{-1} in 1 M KOH electrolyte. Table 4 lists the electrochemical measurements recorded before and after the stabilization test. The spectra shown in Fig. 5(a) depict the changes in the impedance of CCO-0.75 with increasing polarization cycles. From the values listed in Table 4, it can be seen that the largest change (+ 29%) in the R_{ct} of CCO-0.75 occurred after subjecting the electrode to 500 stability cycles. Thereafter, the charge transfer resistance increased marginally by 4–8%. From the cyclic voltammograms from 1.22 to 1.57 (*vs. RHE*) depicted in Fig. 5(b), it can be deduced that the stability testing did not change the anodic peak position significantly even after 2000 cycles of polarization. Moreover, the shift on the onset potential and the potential at 10 mA cm^{-2}, which can be seen in the LSV curves in Fig. 5(c), followed the same observation as that in the impedance spectra. Initially, an 8% increase in the onset potential was recorded after 500 cycles. Then, the difference narrowed down to as low as 1% after 2000 stability cycles. Overall, the observed increase in the potential at the onset of OER and at 10 mA cm^{-2} increased by 15 and 9% after 2000 stability cycles, respectively. Nevertheless, CCO-0.75 exhibited good stability even after 2000 cycles of polarization from 1.22 to 0.57 V vs. Ag/AgCl because the observed increase in the overpotentials were offset by the enhancement of the kinetics of the reaction. This is as evidenced by the reduction in the calculated Tafel slopes from 86 to 77 mV dec^{-1}, as shown in Fig. 5(d). Fig. S8(a) shows the XRD pattern of the CCO-0.75 electrode after the stability testing. From this figure, it can be seen that the structure of the catalyst was retained, and that the CCO-0.75 electrode is still composed of a mixture of spinel Cu-doped Co_3O_4 and monoclinic CuO. From the FESEM images of the CCO-0.75 electrode taken after the stability test in Fig. S8(b), it can be seen that the catalyst retained its urchin-like

microsphere morphology. Furthermore, the nanowires forming these urchin-like structures were consequently formed by interconnected particles, as depicted in Fig. S8(c).

3.4. Alkaline anion exchange membrane water electrolyzer performance

Fig. 6(a) shows the polarization curves of CCO-0.75 in 1 M KOH recorded at 20 and 60 °C. The cell voltage required to reach 100 mA cm^{-2} at 20 and 60 °C were 1.74 and 1.65 V (*vs. RHE*), respectively. This shows a voltage shift of around 10 mV as the operating temperature was increased, which implies the expected improvement of the performance of the cell at higher temperatures. At elevated operating temperatures, the area-specific resistance of the electrodes decreases, which makes the system more conductive and active for water electrolysis [79].

The performance of the loose powder, urchin-like CCO-0.75 electrocatalyst in an AAEMWE is then compared to those of Cu-doped cobalt oxide thin films previously reported [6,50]. The membrane electrode assembly (MEA) in [6] and [48] consisted of a Ni on carbon GDL cathode, mixed Cu–Co oxide thin film on CFP anode, and a commercial alkaline anion exchange embrane Fumapem® FAA-3-50 (Fuel Cell Store). The Cu–Co oxide thin films used in both reports were deposited onto CFP substrates through magnetron sputtering followed by annealing at 500 °C for 2 h. The Co-to-Cu atomic ratio in both films was 1.8. These mixed Cu–Co oxide films are composed of tiny aggregates grown externally on the surface of the carbon fibers [6,50]. Fig. 6(b) shows the cell voltage required to reach 100 mA cm^{-2} in 1 M KOH using CCO-0.75||Pt/C cell utilized in this study, in comparison to that required for CCO thin film||Ni [6] and $Cu_xCo_{3-x}O_4$ ultrathin films||Ni [50]. From this figure, it can be seen that CCO-0.75 performed better than the other Cu–Co oxide-based electrocatalysts mentioned [6,50]. CCO-0.75||Pt/C recorded a voltage about 23 and 14% lower than $Cu_xCo_{3-x}O_4$ ultrathin films||Ni and mixed Cu–Co oxide film||Ni, respectively. The cell voltage recorded for CCO-0.75||Pt/C in this study even at room temperature is lower than that recorded for the other above-mentioned

catalysts in elevated temperatures (30–70 °C). This proves the advantage of using a hierarchical, urchin-like catalyst. This catalyst morphology exhibits a large surface area and ensures that mass transfer loss in the high-potential area is minimal. This characteristic makes more active sites available for the electrochemical processes to occur; hence favoring the catalysis of the oxygen evolution reaction at the anode of the AAEMWE. [49,86]. The performance of the CCO-0.75‖Pt/C cell used herein is also compared to that of the IrO_2‖Pt/C cell in [51]. For such cell, the anode is made up of commercially available IrO_2 catalyst (Sigma-Aldrich, 99.99% trace metal basis) on Ni foam with an approximate loading of 4 mg cm^{-2}. From Fig. 6(b), the required cell potential to reach 100 mA cm^{-2} recorded at 60 °C for the CCO-0.75‖Pt/C cell utilized in this study compares favorably to that recorded for an IrO_2‖Pt/C cell (1.52 V) at 45 °C. This proves the fair performance of CCO-0.75 as an electrocatalyst for the oxygen evolution reaction in alkaline anion exchange membrane water electrolyzers.
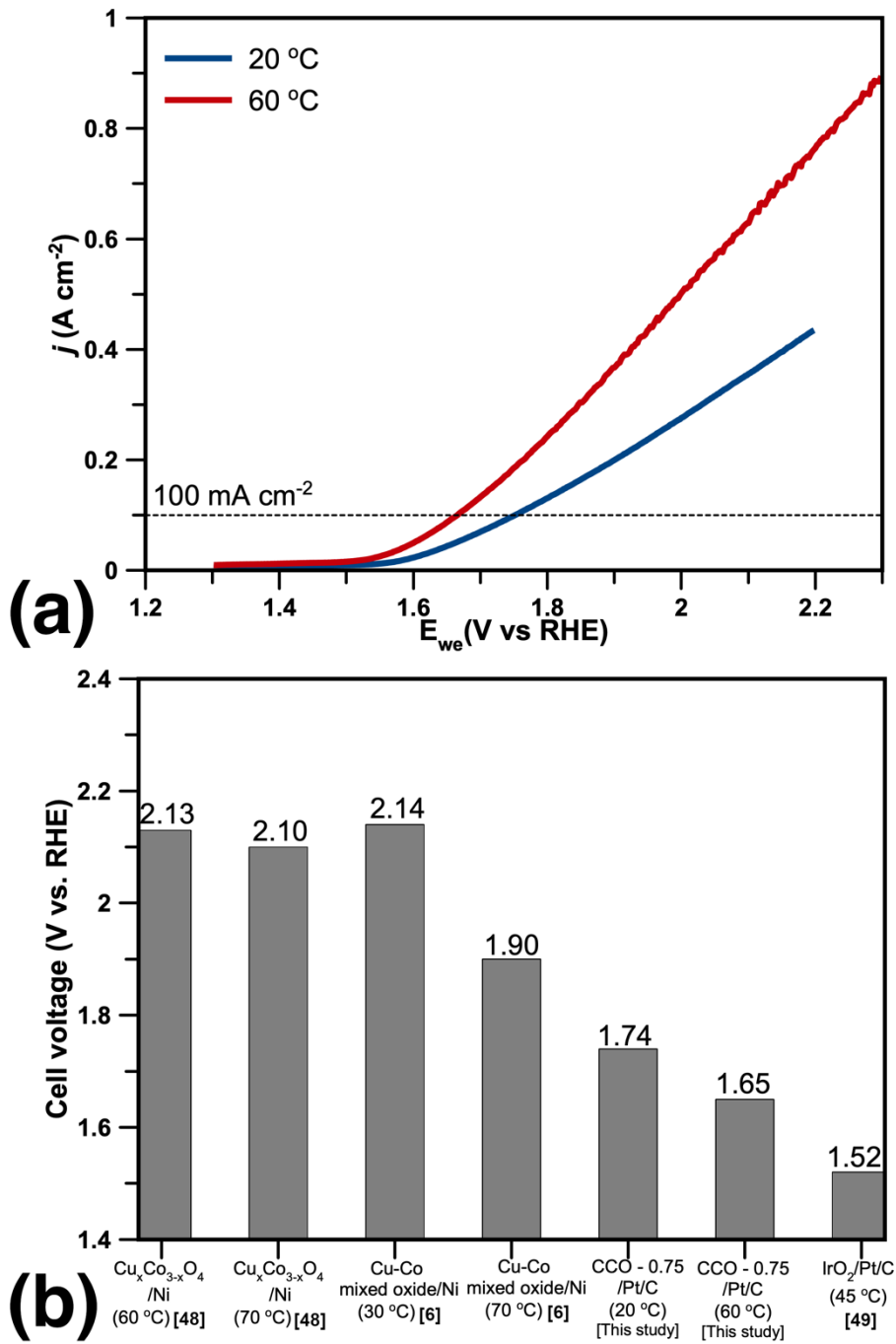
Figure 6. (a) Polarization curves of AAEMWE cell using CCO-0.75 on Ti GDL (2 mg cm^{-2}) anode and Pt/C on carbon GDL (0.4 mg cm^{-2}) cathode in 1 M KOH at 20 and 60 °C, and (b) comparison of the CCO-0.75‖Pt/C with other AAEMWE cells using Cu–Co oxide thin films[6,48] and commercially available IrO$_2$ catalysts.[49]

4. Conclusion

In summary, hierarchical, spinel undoped and Cu-doped Co_3O_4 catalysts for OER in alkaline water electrolysis were prepared through ethanol-assisted hydrothermal method. Five compositions of $Cu_xCo_{3-x}O_4$ (x = 0, 0.25, 0.5, 0.75, and 1) were prepared to study the effect of increasing Cu-concentration on the morphology, structure, and OER catalysis performance of Co_3O_4. SEM revealed that all the synthesized samples, regardless of dopant concentration, exhibited a hierarchical urchin-like morphology. The micro urchins are composed of nanowires, which became finer with increasing amount of Cu. XRD results showed that Cu-doping did not result in the alteration of the spinel structure of Co_3O_4. However, at Cu-doping at x = 0.75 and 1, a secondary, monoclinic CuO phase was produced. BET measurements revealed that Cu-doping resulted in an increase in the specific surface area of the powder produced after the hydrothermal treatment and calcination. The observed increase in the BET specific surface areas calculated were supported by the decreasing crystallite sizes with increasing Cu-dopant concentration determined from the XRD results. This is to minimize the lattice strain induced by the introduction of the dopant Cu^{2+} ions onto the spinel Co_3O_4 lattice. Half-cell activity testing revealed that Cu-doped samples performed better than the undoped Co_3O_4 catalysts. However, activity enhancement was offset beyond x = 0.75, probably due to the increased production of the resistive CuO phase at x = 1. $Cu_xCo_{3-x}O_4$ catalyst with x = 0.75 (CCO-0.75) required only 385 mV to reach 10 mA cm^{-2} in 1 M KOH electrolyte. CCO-0.75 also showed fair stability, having only recorded a 9% increase in this parameter after 2000 cycles of polarization. SEM imaging showed that the urchin-like morphology of CCO-0.75 was retained after the stability test. XRD results also showed that the spinel structure remained unaltered. An alkaline anion exchange membrane water electrolyzer was assembled using CCO-0.75 on Ti GDL as the anode, Pt/C on carbon GDL as the cathode, and LDPE–VBC–TMA as the membrane. The assembled CCO-0.75‖Pt/C cell recorded a cell voltage of 1.74,

30

and 1.65 V to reach 100 mA cm^{-2} at 20, and 60 °C in 1 M KOH electrolyte. This compares favorably to those recorded for Cu–Co oxide thin films reported in literature.

In this study, the fair activity of $Cu_xCo_{3-x}O_4$ towards OER catalysis in alkaline medium was established. The field of OER catalysis is highly competitive, with various catalysts and materials being explored. Cu-doped Co_3O_4 must compete with other emerging catalysts for widespread adoption. As in other materials, Cu can be susceptible to corrosion in alkaline environments over extended periods, which may affect the long-term stability of the catalyst. Consequently, the active sites in $Cu_xCo_{3-x}O_4$ may degrade over time, thereby reducing its catalytic efficiency. Another limitation is the potential challenge of scaling up the use of $Cu_xCo_{3-x}O_4$ catalysts on laboratory experiments to large-scale industrial applications, which involves addressing uniformity and scalability of catalyst synthesis. Despite these challenges, $Cu_xCo_{3-x}O_4$ still exhibits an immense potential as a low-cost OER catalyst that can improve the efficiency and sustainability of hydrogen production technologies. Addressing these limitations through ongoing research and development efforts can help maximize its potential for water electrolyzer applications.

For future research, three key points can significantly drive advancements in OER catalysis using $Cu_xCo_{3-x}O_4$. First, the development of advanced synthesis methods is crucial, focusing on creating high-purity Cu-doped Co_3O_4 catalysts, even at high Cu concentrations (x > 0.5), to prevent the formation of impurities like CuO. Secondly, performing density functional theory (DFT) calculations can provide a comprehensive understanding of the interaction between the catalyst and OH$^-$ ions, revealing the catalytic mechanism, which can guide the exploration of alternative strategies for performance enhancement. Lastly, *in situ* or *operando* characterization techniques can determine the real active species and catalytic sites, facilitating the understanding of the catalytic mechanism and offering valuable insights into novel directions for optimizing catalyst design and performance.

CRediT authorship contribution statement

Rose Anne E. Acedera: Writing - original draft. Gaurav Gupta: Writing - original draft, review & editing. Kodai Kawano: Writing – original draft. Yagi Shunsuke: Writing – review & editing. Mohamed Mamlouk: Writing - review & editing. Mary Donnabelle L. Balela: Writing - review & editing.

Declaration of competing interest

The authors declare that they have no known competing financial interests or personal relationships that could have appeared to influence the work reported in this paper.

References

1   E. Ghiani and G. Pisano, *Impact of Renewable Energy Sources and Energy Storage Technologies on the Operation and Planning of Smart Distribution Networks*, Elsevier Inc., 2018.

2   Y. Liu and J. liang Du, *J Clean Prod*, 2020, **277**, 122183.

3   Z. Yan, J. L. Hitt, J. A. Turner and T. E. Mallouk, *Proc Natl Acad Sci U S A*, 2020, **117**, 12558–12563.

4   C. Coutanceau, S. Baranton and T. Audichon, *Hydrogen Electrochemical Production*, 2017, 1–6.

5   T. M. Letcher, *Storing Energy - With Special Reference to Renewable Energy Sources*, 2016.

6   E. López-Fernández, J. Gil-Rostra, J. P. Espinós, A. R. González-Elipe, F. Yubero and A. de Lucas-Consuegra, *J Power Sources*, 2019, **415**, 136–144.

7   X. Yan, X. Yang, X. Su, L. Gao, J. Zhao, L. Hu, M. Di, T. Li, X. Ruan and G. He, *J Power Sources*, 2020, **480**, 228805.

8   K. Zeng and D. Zhang, *Prog Energy Combust Sci*, 2010, **36**, 307–326.

9   I. Vincent and D. Bessarabov, *Renewable and Sustainable Energy Reviews*, 2018, **81**, 1690–1704.

10   A. Farzaneh, E. K. Goharshadi, H. Gharibi, N. Saghatoleslami and H. Ahmadzadeh, *Electrochim Acta*, 2019, **306**, 220–228.

11   X. Wu and K. Scott, *J Mater Chem*, 2011, **21**, 12344–12351.

12   E. Rasten, G. Hagen and R. Tunold, *Electrochim Acta*, 2003, **48**, 3945–3952.

13   A. T. Marshall and L. Vaisson-Béthune, *Electrochem commun*, 2015, **61**, 23–26.

14   S. Cherevko, T. Reier, A. R. Zeradjanin, Z. Pawolek, P. Strasser and K. J. J. Mayrhofer, *Electrochem commun*, 2014, **48**, 81–85.

15   J. Ahmed and Y. Mao, *Electrochim Acta*, 2016, **212**, 686–693.

16   Z. Ma, Y. Zhang, S. Liu, W. Xu, L. Wu, Y. C. Hsieh, P. Liu, Y. Zhu, K. Sasaki, J. N. Renner, K. E. Ayers, R. R. Adzic and J. X. Wang, *Journal of Electroanalytical Chemistry*, 2018, **819**, 296–305.

17   S. Siracusano, V. Baglio, A. Stassi, R. Ornelas, V. Antonucci and A. S. Aric, *Int J Hydrogen Energy*, 2011, **36**, 7822–7831.

18   M. H. P. Santana and L. A. De Faria, *Electrochim Acta*, 2006, **51**, 3578–3585.

19   J. Jirkovský, M. Makarova and P. Krtil, *Electrochem commun*, 2006, **8**, 1417–1422.

20   M. Karimi-Nazarabad and E. K. Goharshadi, *Journal of Electroanalytical Chemistry*, 2022, **904**, 115933.

21   Y. Lee, J. Suntivich, K. J. May, E. E. Perry and Y. Shao-Horn, *Journal of Physical Chemistry Letters*, 2012, **3**, 399–404.

22   S.-Y. Lee, I.-S. Kim, H.-S. Cho, C.-H. Kim and Y.-K. Lee, *Appl Catal B*, 2021, **284**, 119729.

23   D. C. Nguyen, T. L. Luyen Doan, S. Prabhakaran, D. T. Tran, D. H. Kim, N. H. Kim and J. H. Lee, *Nano Energy*, 2021, 105750.

24   S. Wang, G. Zhou, J. Lv, Y. Ma, Y. Wang, C. Hu, J. Zhang, J. Yang, G. He, M. Zhang, M. Zhao, X. Chen and L. Yang, *Journal of Physics and Chemistry of Solids*, 2021, **148**, 109696.

25   P. Teppor, R. Jäger, M. Paalo, R. Palm, O. Volobujeva, E. Härk, Z. Kochovski, T. Romann, R. Härmas, J. Aruväli, A. Kikas and E. Lust, *Electrochem commun*, 2020, **113**, 106700.

26   Y. V. Kaneti, Y. Guo, N. L. W. Septiani, M. Iqbal, X. Jiang, T. Takei, B. Yuliarto, Z. A. Alothman, D. Golberg and Y. Yamauchi, *Chemical Engineering Journal*, 2021, **405**, 126580.

27   D. Huo, F. Song, J. Hu, J. Yuan, L. Niu and A. Wang, *Int J Hydrogen Energy*, , DOI:https://doi.org/10.1016/j.ijhydene.2020.12.050.

28   G. Yuan, J. Bai, L. Zhang, X. Chen and L. Ren, *Appl Catal B*, 2021, **284**, 119693.

29   J. Li, G. Liu, J. Fu, G. Jiang, D. Luo, F. M. Hassan, J. Zhang, Y.-P. Deng, P. Xu, L. Ricardez-Sandoval and Z. Chen, *J Catal*, 2018, **367**, 43–52.

30   Y. Li, Q. Guo, Y. Jiang, W. Shen, M. Li and R. He, *Chinese Chemical Letters*, , DOI:https://doi.org/10.1016/j.cclet.2020.05.012.

31   R. Zhang, S. Cheng, N. Li and W. Ke, *Appl Surf Sci*, 2020, **503**, 144146.

32   Y. Dong, S. Komarneni, F. Zhang, N. Wang, M. Terrones, W. Hu and W. Huang, *Appl Catal B*, 2020, **263**, 118343.

33   S. H. Kim, Y. S. Park, C. Kim, I. Y. Kwon, J. Lee, H. Jin, Y. S. Lee, S. M. Choi and Y. Kim, *Energy Reports*, 2020, **6**, 248–254.

34   X. Ma, P. Wei, Y. Yang, H. Kang, D. Guo and L. Liu, *Mater Today Commun*, 2019, **20**, 100596.

35   L. Yang, Z. Liu, S. Zhu, L. Feng and W. Xing, *Materials Today Physics*, 2021, **16**, 100292.

36   X.-M. Liu, X. Cui, K. Dastafkan, H.-F. Wang, C. Tang, C. Zhao, A. Chen, C. He, M. Han and Q. Zhang, *Journal of Energy Chemistry*, 2021, **53**, 290–302.

37   W. Liu, J. Han, I. Yamada and S. Yagi, *J Catal*, 2021, **394**, 50–57.

38   A. Singhal, A. Bisht and S. Irusta, *Journal of Electroanalytical Chemistry*, 2018, **823**, 482–491.

39   B. Chi, H. Lin and J. Li, *Int J Hydrogen Energy*, 2008, **33**, 4763–4768.

40 S. Fareed, R. Medwal, J. V. Vas, I. A. Khan, R. S. Rawat and M. A. Rafiq, *Ceram Int*, 2020, **46**, 9498–9506.

41 M. Aadil, G. Nazik, S. Zulfiqar, I. Shakir, M. F. Aly Aboud, P. O. Agboola, S. Haider and M. F. Warsi, *Ceram Int*, , DOI:https://doi.org/10.1016/j.ceramint.2020.12.048.

42 P. Cheng, F. Dang, Y. Wang, J. Gao, L. Xu, C. Wang, L. Lv, X. Li, B. Zhang and B. Liu, *Sens Actuators B Chem*, 2021, **328**, 129028.

43 C. L. I. Flores and M. D. L. Balela, *Journal of Solid State Electrochemistry*, 2020, **24**, 891–904.

44 I. Nikolov, R. Darkaoui, E. Zhecheva, R. Stoyanova, N. Dimitrov and T. Vitanov, *Journal of Electroanalytical Chemistry*, 1997, **429**, 157–168.

45 H. Chen, J. Wang, F. Liao, X. Han, Y. Zhang, C. Xu and L. Gao, *Ceram Int*, 2019, **45**, 11876–11882.

46 F. Qu, N. Zhang, D. Liu, S. Zhang, B. Talluri, Y. Zheng, T. Thomas, R. Zhao, S. Ruan and M. Yang, *Sens Actuators B Chem*, 2020, **308**, 127651.

47 A. La Rosa-Toro, R. Berenguer, C. Quijada, F. Montilla, E. Morallón and J. L. Vázquez, *Journal of Physical Chemistry B*, 2006, **110**, 24021–24029.

48 A. Lakehal, B. Benrabah, A. Bouaza, C. Dalache and B. Hadj, *Chinese Journal of Physics*, 2018, **56**, 1845–1852.

49 R. A. E. Acedera and M. D. L. Balela, *IOP Conf Ser Mater Sci Eng*, , DOI:10.1088/1757-899X/617/1/012004.

50 E. López-Fernández, J. Gil-Rostra, C. Escudero, I. J. Villar-García, F. Yubero, A. de Lucas Consuegra and A. R. González-Elipe, *J Power Sources*, , DOI:10.1016/j.jpowsour.2020.229217.

51 Y. S. Park, M. J. Jang, J. Jeong, S. M. Park, X. Wang, M. H. Seo, S. M. Choi and J. Yang, *ACS Sustain Chem Eng*, , DOI:10.1021/acssuschemeng.9b06767.

52   M. J. Jang, J. Yang, J. Lee, Y. S. Park, J. Jeong, S. M. Park, J. Y. Jeong, Y. Yin, M. H. Seo, S. M. Choi and K. H. Lee, *J Mater Chem A Mater*, 2020, **8**, 4290–4299.

53   M. Karimi-Nazarabad, E. K. Goharshadi and H.-S. Sajjadizadeh, *The Journal of Physical Chemistry C*, 2022, **126**, 8327–8336.

54   P. Poix, *Bull Soc. Chim., France*, 1965, **5**, 1085–1087.

55   G. Gupta, K. Scott and M. Mamlouk, *Fuel Cells*, 2018, **18**, 137–147.

56   G. Gupta, K. Scott and M. Mamlouk, *J Power Sources*, 2018, **375**, 387–396.

57   Q. Zhang, Z. D. Wei, C. Liu, X. Liu, X. Q. Qi, S. G. Chen, W. Ding, Y. Ma, F. Shi and Y. M. Zhou, *Int J Hydrogen Energy*, 2012, **37**, 822–830.

58   V. Ambardekar, S. Sahoo, D. K. Srivastava, S. B. Majumder and P. P. Bandyopadhyay, *Sens Actuators B Chem*, 129404.

59   Y. S. Park, C. S. Park, C. H. Kim, Y. Do Kim, S. Park and J. H. Lee, 2016, **69**, 1187–1190.

60   N. Fradette and B. Marsan, .

61   R. N. Singh, J. P. Pandey, N. K. Singh, B. Lal, P. Chartier and J. F. Koenig, *Electrochim Acta*, 2000, **45**, 1911–1919.

62   R. A. E. Acedera, G. Gupta, M. Mamlouk and M. D. L. Balela, *J Alloys Compd*, 2020, **836**, 154919.

63   G. Hao, W. Wang, G. Gao, Q. Zhao and J. Li, *Journal of Energy Chemistry*, 2015, **24**, 271–277.

64   S. A. Makhlouf, Z. H. Bakr, K. I. Aly and M. S. Moustafa, *Superlattices Microstruct*, 2013, **64**, 107–117.

65   A. Tamayo, M. A. Rodríguez, C. Arroyo, J. Beltran-Heredia and F. Rubio, *J Eur Ceram Soc*, 2018, **38**, 1583–1591.

66   L. L. Ding, L. C. Xue, Z. Z. Li, S. Q. Li, G. D. Tang, W. H. Qi, L. Q. Wu and X. S. Ge, *AIP Adv*, , DOI:10.1063/1.4966253.

67   R. Sagheer, M. Khalil, V. Abbas, Z. N. Kayani, U. Tariq and F. Ashraf, *Optik (Stuttg)*, , DOI:10.1016/j.ijleo.2019.163428.

68   R. D. Shannon and C. T. Prewitt, *Journal of Inorganic and Nuclear Chemistry*, 1970, **32**, 1427–1441.

69   R. D. Shannon and C. T. Prewitt, *Acta Crystallogr*, 1969, 925–946.

70   R. Li, D. Zhou, J. Luo, W. Xu, J. Li, S. Li, P. Cheng and D. Yuan, *J Power Sources*, 2017, **341**, 250–256.

71   S. Shafique, S. Yang, Y. T. Woldu and Y. Wang, *Sens Actuators A Phys*, 2019, **288**, 107–116.

72   F. Ambroz, T. J. Macdonald, V. Martis and I. P. Parkin, *Small Methods*, 2018, **2**, 1800173.

73   S. Wang, H. Xu, L. Qian, X. Jia, J. Wang, Y. Liu and W. H. Tang, *J Solid State Chem*, 2009, **182**, 1088–1093.

74   S. Li, Y. Wang, J. Sun, Y. Zhang, C. Xu and H. Chen, *J Alloys Compd*, 2020, **821**, 153507.

75   E. Umeshbabu, G. Rajeshkhanna and G. R. Rao, *Int J Hydrogen Energy*, 2014, **39**, 15627–15638.

76   H. Chen and C. Xu, *Mater Lett*, 2016, **166**, 188–191.

77   S. H. Guo, P. W. Yuan, J. Wang, W. Q. Chen, K. Y. Ma, F. Liu and J. P. Cheng, *Journal of Electroanalytical Chemistry*, 2017, **807**, 10–18.

78   S. Liu, K. S. Hui, K. N. Hui, V. V Jadhav, Q. X. Xia, J. M. Yun, Y. R. Cho, R. S. Mane and K. H. Kim, *Electrochim Acta*, 2016, **188**, 898–908.

79   G. Gupta, K. Selvakumar, M. Mamlouk, N. Lakshminarasimhan and S. M. Senthil Kumar, *J Power Sources*, 2020, **461**, 228131.

80   X. Wu and K. Scott, 2013, **8**, 1–7.

81   A. H. A. Monteverde Videla, P. Stelmachowski, G. Ercolino and S. Specchia, *J Appl Electrochem*, 2017, **47**, 295–304.

82   Y. Zhang, K. Xu, B. Zhang, S. Guan, X. Fu and Z. Peng, *J Alloys Compd*, 2020, 158047.

83   X. Han, C. Yu, H. Huang, W. Guo, C. Zhao, H. Huang, S. Li, Z. Liu, X. Tan, Z. Gao, J. Yu and J. Qiu, *Nano Energy*, 2019, **62**, 136–143.

84   Y. Xu, M. A. Khan, Z. Chen, C. Chen, L. Zhang, D. Ye, K. Zhao, H. Zhao, X. A. Sun and J. Zhang, *Mater Today Energy*, 2020, **18**, 100564.

85   P. Connor, J. Schuch, B. Kaiser and W. Jaegermann, *Zeitschrift fur Physikalische Chemie*, 2020, **234**, 979–994.

86   S. Liu, *Int J Electrochem Sci*, 2018, **13**, 3843–3854.